A Methodology for Luminance Map Retrieval using Airborne Hyperspectral and Photogrammetric Data

Luca Pipia, Ramon Alamús, Anna Tardà, Fernando Pérez, Vicenç Palà, Jordi Corbera

Institut Cartogràfic i Geològic de Catalunya (ICGC), Parc de Montjuïc, Barcelona, Spain E-08038

ABSTRACT

This paper puts forward a methodology developed at the Institut Cartogràfic i Geològic de Catalunya (ICGC) to quantify upwelling light flux using hyperspectral and photogrammetric airborne data. The work was carried out in the frame of a demonstrative study requested by the municipality of Sant Cugat del Vallès, in the vicinity of Barcelona (Spain), and aimed to envisage a new approach to assess artificial lighting policies and actions as alternative to field campaigns. Hyperspectral and high resolution multispectral/panchromatic data were acquired simultaneously over urban areas. In order to avoid moon light contributions, data were acquired during the first days of new moon phase. Hyperspectral data were radiometrically calibrated. Then, National Center for Environmental Prediction (NCEP) atmospheric profiles were employed to estimate the actual Column Water Vapor (CWV) to be passed to ModTran5.0 for the atmospheric transmissivity τ calculation. At-the-ground radiance was finally integrated using the photopic sensitivity curve to generate a luminance map (cdm^{-2}) of the flown area by mosaicking the different flight tracks. In an attempt to improve the spatial resolution and enhance the dynamic range of the luminance map, a sensor-fusion strategy was finally looked into. DMC Photogrammetric data acquired simultaneously to hyperspectral information were converted into at-the-ground radiance and upscaled to CASI spatial resolution. High-resolution (HR) luminance maps with enhanced dynamic range were finally generated by linearly fitting up-scaled DMC mosaics to the CASI-based luminance information. In the end, a preliminary assessment of the methodology is carried out using non-simultaneous in-situ measurements.

Keywords: Light pollution, hyperspectral data, photogrammetric data, photopic filter, luminance, luminous flux, sensor fusion, sensor cross-calibration.

1. INTRODUCTION

Nocturnal light pollution is a side effect of industrial civilization. Also known as photo-pollution or luminous pollution, this term usually accounts for the excessive, misdirected or undesired artificial light that may be observed over an area of interest. Its sources include buildings exterior and interior lighting, advertising, commercial properties, offices, illuminated sporting venues and, obviously, streetlights. In the last years, debates about energy efficient use as well as energy conservation stressed the importance of monitoring artificial lightening at global, regional and local scale. The former position advocates the need to use energy more efficiently, that is, using less energy for the same level of service. The latter one exhorts to address the light pollution issue by changing the habits of society, using lighting more efficiently, with less waste and less creation of unwanted or unneeded illumination. Being the final goal to be pursued the reduction of either the costs involved in the private or public area illumination or the impact on the environment, having at disposal a reliable tool to describe quantitatively the amount of artificial light radiation characterizing the earth surface becomes crucial. On the one hand, it makes it possible to detect light wastes or even outlawed light hotspots. On the other hand, it provides a quantitative descriptor to assess the effectiveness of policies and actions taken to deal with the aforementioned issues.

The spectral sensitivity of human visual perception of brightness is described by the photopic luminosity function defined by the Commission Internationale de l'Éclairage (CIE) [1][2]. In essence, the photopic curve indicates the sensitivity of human eye to incoming light radiation at different wavelengths. It follows that light meters measure the amount of visible light in a given areas reproducing the human eye response. From this point of view, hyperspectral Vis-NIR sensors are versatile devices because they are able to combine the advantages of a synoptic view achieved from airborne or satellite platforms, and to provide a fine-sampled description of the imaged scene spectrum.

In the literature, hyperspectral and multispectral airborne sensors were often used for nocturnal image analysis. Yet, all these studies were focused on the detection of artificial light sources or classification based on specific spectral signature

detection [3][4][5][6]. On the contrary, studies based on space-borne night imaging mainly dealt with the analysis of global urban extent at global and regional scale [8]. The reason is threefold: the fewer bands available for spectral signature identification; the coarse spatial resolution of all operational sensors providing night images (about 3 km for Defense Military Satellite Program (DMSP) [7], 740 m for the Visible Infrared Imaging Radiometer Suite (VIIRS) on-board SUOMI NPP platform [9]); the reduced dynamic range of night acquisitions. Recently, the commercial satellite EROS-B was tasked to acquire night-time light images over Brisbane, Australia, for the detection of arterial roads and commercial/service areas [10]. The study showed the fine spatial resolution of nigth images that are acquired by diurnal-devised satellite sensors. At the same time, it pointed out their limitations when it comes to describing low levels of brightness. Finally, all these previous studies lacked any quantitative characterization of the imaged light flux information, meaning that no quantitative descriptor to assess the effectiveness of any energy efficiency policies and actions was finally provided.

In an attempt to deal with this issue, a simple model for the quantitative characterization of the luminous flux at a local scale was developed at the Institut Cartogràfic and Geològic de Catalunya (ICGC). The paper is organized as follows. Section 2 briefly describes the area of interest and the flight main information. Section 3 details the main characteristics of the hyperspectral sensor, the CASI550, used for this first luminance parameter retrieval. In Section 4, the result in terms of luminance map is shown and the limitations of the approach in terms of spatial resolution and dynamic range are pointed out. In Section 5, the DMC photogrammetric sensor, which was flown simultaneously to CASI550 over the area of study, is introduced. The need to substitute the failing steps of the standard data processing by homemade processing software and to remove readout noise pattern is also reported. The high resolution maps obtained by fusing the two sensors are finally presented in Section 6. In Section 7, a preliminary assessment of the methodology is carried out using non-simultaneous in-situ measurements acquired using a handheld luminance meter mounted on an aerial work platform. In last Section, overall conclusions about the study presented in the paper are drawn and future works are envisaged.

2.   STUDY AREA

During the last years, the municipal administration of Sant Cugat del Vallès, a small town located north-west of Barcelona (Spain), was very active in promoting efficient artificial lighting policies. Yet, the in-situ assessment of their effects on the public areas was time-consuming and unable to provide a synoptic view of the whole municipality. In order to overcome this limitation, they funded a pilot study carried out by ICGC aiming to achieve this goal using hyperspectral and photogrammetric airborne data. To cover the whole area of interest, approximately 48.2 Km^2, parameters such as the sensors field of view (see Table 1 and Table 2), the swath overlapping percentage for hole-free radiance coverage and especially the minimum altitude permitted for night flights over urban areas were taken into account. Accordingly, 12 flight tracks were planned at approximately 2200m AGL, as shown in Figure 1. The positive and negative numbers of each track define where the acquisition starts and ends, respectively. The data were acquired on 2/2/2014, from 23:25pm to 00:53 am next day.

Figure 1 Flight tracks over the area of interest of Sant Cugat, Barcelona, Spain.

3. CASI 550 AND METHODOLOGY

The CASI-550 is a VisNIR pushbroom imager with a reflection grating and a two-dimensional CCD (charge coupled device) solid-state array detector, manufactured by Itres [11]. This instrument has been regularly operated by ICGC since 1994. The instrument operates by looking down in a fixed direction and imaging successive lines of the flown scene, building up a two-dimensional image as the platform moves forward. One dimension of the CCD covers the across-track spatial direction; the other one accounts for the spectral domain. CASI-550 can be operated in a mode called "spatial", where non-overlapping bans with any width can be configured. Another possible acquisition mode is "*enhanced*", chosen for this study, which divides the spectral window 400 nm – 900 nm in a set of sub-spectral bands, all of them with the same spectral width. Table 1 summarizes the main configuration parameters used for the night flights over Sant Cugat del Vallès, as well as some flight information.

FOV [deg]	40
# of FOV Pixels	550
# of Spectral bands	96
Spectral range [nm]	409.65 – 954.83
Spectral resolution [nm]	5.74
Data Depth	14 bits
Height above ground [m]	2243
GSD [m]	3x3
Swath overlapping	40%

Table 1: CASI 550 acquisition information and flight parameters in Sant Cugat.

The hyperspectral information collected by CASI 550 at pixel level is essentially a spectral sampling of the VisNIR radiation emitted by the surface and entering the sensor through a narrow solid angle. It is known that the radiation measured during the day is the sum of direct, indirect and scattered contributions arising from the interaction of sun light with the atmosphere and the surface. It is crucial to take into account all these contributions if the reflectivity signature of each pixel has to be retrieved. On the contrary, if one is interested in the estimate of the at-the-ground radiance the model simplifies because the only contribution to be compensated for is the path radiance. Moving to night-time acquisition, the goal becomes the estimation of the at-the-ground radiance due to just the artificial illumination. Accordingly, if any extraterrestrial light source is avoid by selecting specific time windows as for instance new moon phase, it is possible to express the *at-the-sensor* incoming spectral radiation as

$$L^{@SENSOR}(\lambda) = L^{@GROUND}(\lambda)\tau(\lambda) + L^*(\lambda) + L_n(\lambda) \tag{1}$$

where $\tau(\lambda)$ is the spectral transmissivity of the atmosphere calculated at the plane altitude, $L^*(\lambda)$ accounts for the artificial light atmosphere scattering [12] and L_n for a generic wave-dependent additive noise.

In order to convert the radiance information into luminance, some key concept must be introduced. In general, a luminosity function describes the average spectral sensitivity of human visual perception of brightness. There exist two luminosity functions: the photopic one, approximating human eye response to day-time light levels, and the scotopic one, accounting for eye response to low light levels. A pictorial description of the curves is given in Figure 2. The CIE luminosity function $V(\lambda)$ is the standard function to be used to convert radiant energy into photopic luminous (i.e., visible) energy established by the Commission Internationale de l'Éclairage (CIE) [1][2]. The photopic flux F for each pixel of the observed surface, measured in $[lm\ m^{-2}sr^{-1}]$ or $[cdm^{-2}]$, is then given by

$$F = K\int_0^\infty L^{@GROUND}(\lambda)V(\lambda)d\lambda = K\int_0^\infty \frac{L^{@SENSOR}(\lambda) - L^*(\lambda) - L_n(\lambda)}{\tau(\lambda)}V(\lambda)d\lambda \tag{2}$$

where K=683.002 lm/W. Taking into account the discrete spatial/spectral sampling carried out any digital imager and the geometry dependence of the atmospheric effects, equation (2) may be rewritten as
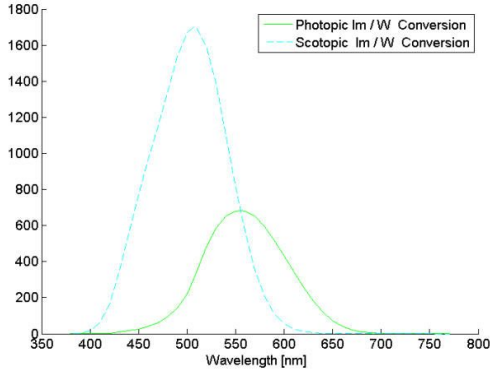
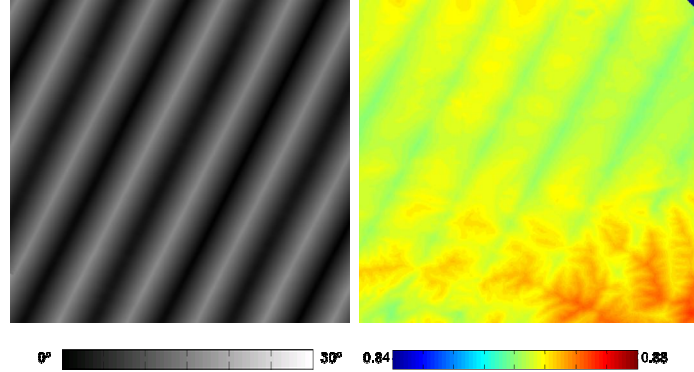**Figure 2** Photopic (green) and Scotopic (cyan) luminosity function.

Figure 3 Spatial distribution of zenith angle θ(left) and τ@784 nm -Band 67- (right) over a subarea of Sant Cugat.

$$F(l,c) = K \sum_{i=1}^{N_{Bands}} \frac{L_i^{@\,SENSOR}(l,c) - L_i^*(l,c) - L_{n,i}}{\tau_i(x,y,z,x_s,y_s,z_s,CWV)} V_i \Delta\lambda_i \qquad i = 1,...,N_{bands} \tag{3}$$

where l and c stand for the line and column of the pixel imaging a generic point P at (x,y,z) of the observed scene; (x_s, y_s,z_s) describes the position of the sensor when the point P is sensed; $\Delta\lambda_i$ is the bandwidth of the filter describing the ith hyperspectral band, and V_i is the value of V (λ) integrated by the ith band filter.

Note that equation (3) stresses the dependence of the spectral trasmissivity τ not only on pixel observation geometry, but also to the actual Colum Water Vapor (CWV) of the atmosphere during the acquisition process. With respect to the value of CWV provided by atmospheric simulator standard models, a more truthful estimation of this parameter may be obtained using the National Centers for Environmental Prediction (NCEP) [14] atmospheric profiles. These profiles are calculated at the geographic coordinates of the center of each flight-track, and tied to simultaneous local weather information. Afterwards, a Look-Up-Table (LUT) is constructed using ModTran5.0 [13] considering different values of pixels height and zenith angle. The final value of τ is obtained at pixel level by interpolating the LUT at pixel actual height and zenith angle.

Figure 3 shows an example of the spatial distribution of τ over a subarea of Sant Cugat, calculated at 784 nm (the central wavelength of band 67), and its dependence on the zenith angle. The parallel strips detectable within the τ image correspond to the seamline between contiguous swaths. Over flat areas, these pixels show higher zenith angles, meaning higher optical paths and hence higher attenuation effects.

4. CASI-BASED LUMINANCE MAP

In order to retrieve the luminance information at pixel level, the first step was the radiometric calibration of CASI hyperspectral data. Through this step, the Digital Numbers (DNs) stored for each acquisition line are converted into spectral radiance, measured in $Wcm^{-2}sr^{-1}nm^{-1}$. The accuracy of the quantitative information provided by CASI was previously assessed using the integrating sphere at disposal at ICGC (Figure 4). According to the sphere calibration certificate provided by National Physical Laboratory (NPL) in UK [16], the luminance of the calibrator is 966.45 fL at 1000 fL displayed on the control unit, corresponding to 3318 [cdm^{-2}]. The averaged value retrieved on the pixels of field of view of CASI550 illuminated by the sphere was 3313 [cdm^{-2}], with an absolute error lower than 2‰. This is shown in Figure 5.

Afterwards, temperature, NCEP humidity and pressure vertical profiles were retrieved for each flight track. To estimate the actual CWV, the center of each flight track was assumed as time and space reference of the whole swath. In order to tie the NCEP profiles to the actual atmosphere at the ground, the weather information provided every 30 minutes by the Cendanyola del Vallès XEMA station [15], located at about 7km from the center of the flown area, was used. Then, ModTran5.0 simulations were used out to generate the transmissivity LUTs and a 2D interpolation was finally carried out to calculate the attenuation parameter for each pixel of the imaged scene at each band wavelength.

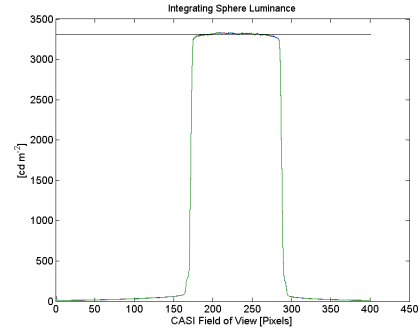**Figure 4** Integrating sphere at ICGC calibrated by NPL.

Figure 5 Theoretical ICGC integrating sphere luminance vs CASI-based retrieved luminance.
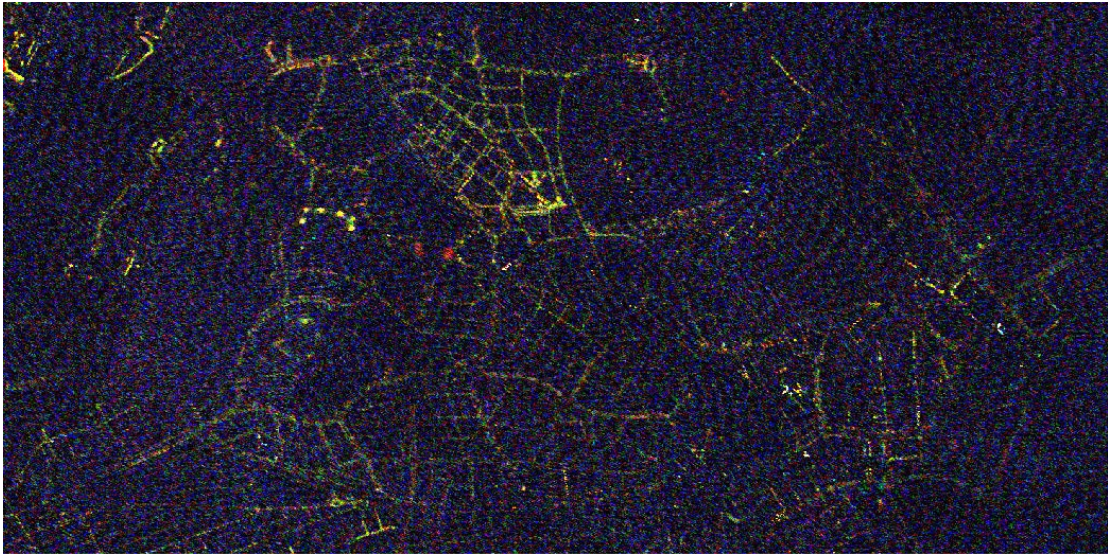

Figure 6 RGB composition of three channels of the 96-band CASI data acquired over Sant Cugat on 2/2/2014.

It is worth pointing out that despite the lower altitude of airborne platform with respect to satellite, low Signal-to-Noise Ratio (SNR) distribution characterized the pixels of most of the bands. In Figure 6, it can be observed the RGB image obtained selecting three bands centered at 819nm, 596nm, and 543nm, which correspond to the artificial lamp signature main peaks where most of energy is concentrated. Only main streets are easily detectable, whereas the street texture is hardly deducible in the rest of the image. Along-track radiometric fluctuations are also present. Note that that these fluctuations are always present in CASI550 measurements, but they are negligible due to the high SNR of diurnal data and the heterogeneity of the sensed scenes. Any attempt to filter them out from night data turned out to be unsatisfactory: the few DNs of information that are available in each band tend to be compromised by the filtering procedure.

In order to integrate the hyperspectral information and retrieve the luminance parameter, expression in (3) was then reviewed. Separating the direct term, equation (3) was rewritten as

$$F(l,c) = K \sum_{i=1}^{N_{Bands}} \frac{L_i^{@\,SENSOR}(l,c)}{\tau_i(x,y,z,x_s,y_s,z_s,CWV)} V_i \Delta\lambda_i - K^*(l,c) - K_n(l,c) = F_0(l,c) - \left[K^*(l,c) + K_n(l,c)\right] \qquad (4)$$

where $K^*(l,c)$ accounts for the global effect of the scattering process onto the luminous flux, $K_n(l,c)$ is the additive noise term. Theoretically, these two terms are related to the observation geometry, which changes from pixel to pixel. Yet, owing to mild topography over the urban area, this dependence was found to be negligible.

Figure 7 Scattering-affected luminous (photopic) flux F_0 retrieved over the urban area of Sant Cugat.

This is observable in Figure 7, which shows the scattering-affected luminance F_0 over the urban area of Sant Cugat del Vallès at 3m spatial resolution. The scattering contributions and the noise term K_n were estimated at once over the dark areas and finally removed from F_0 to achieve a non-biased description of F. The mean value of the two term combination was about 1.9cdm^{-2}. Finally, the along-track striping effects were almost completely compensated for by taking advantage of the higher dynamic range of F, which made it possible to carry out a statistical characterization of these undesired fluctuations along the flight direction.

5. DMC DATA PROCESSING

In an attempt to improve the spatial resolution and enhance the dynamic range of the luminance map, a sensor-fusion strategy was also looked into. Photogrammetric data were taken simultaneously to CASI-550 acquisitions using the DMC camera [17] regularly operated by ICGC for cartographic mapping.

DMC is a high-resolution photogrammetric frame camera, manufactured by Z/I imaging (currently Hexagon), which simultaneously captures one high-resolution (HR) panchromatic and four low-resolution (LR) multi-spectral (red, green, blue and near-infrared) images. The across-track and along-track ratio between multispectral and panchromatic imaging is 1:4. The high resolution image is the result of mosaicking four subimages acquired by four inclined panchromatic camera heads. Each of them covers approximately a quarter of the final image, called virtual image. The four low resolution multi-spectral images in the red, green, blue and near-infrared color bands are acquired with four additional nadir-looking camera heads with a focal length of 25 mm. Note that the four images completely cover the virtual high resolution image. Information concerning the DMC acquisitions over the area of interest is reported in Table 2.

Concerning the DMC data processing, homemade workarounds had to be developed in order to obtain meaningful images to be studied. The reason is related to the maximum exposure time of 33 ms that the camera control SW is able to provide.

FOV [deg]	69.3º (ACT) x 42º(ALT)
# of FOV Pixels (HR)	13824x 7680
# of FOV Pixels (LR)	3072x1920
# of Spectral bands	1(panHR) /4LR
Focal Length [mm]	120(pan)/25(LR)
GSD [m]	0.25(panHR)/1(LR)
Swath overlapping (side/end lap)	70%/70%

Table 2 DMC acquisition information and flight parameters over Sant Cugat del Vallès.
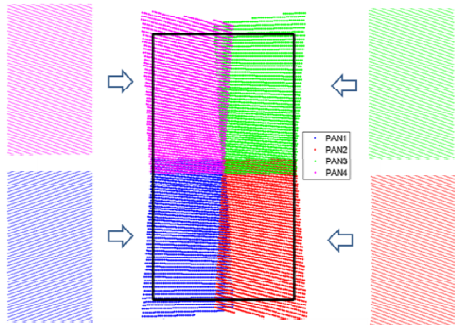
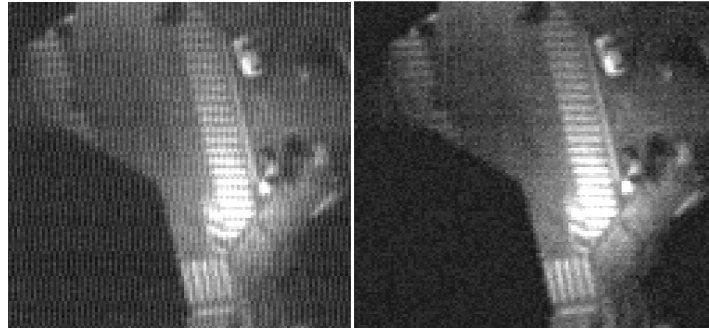**Figure 8** Sketch of the DMC Panchromatic heads projection onto the virtual plane.

Figure 9 Example of electronic noise pattern of panchromatic imaging (left) and the result after the spectral filtering.
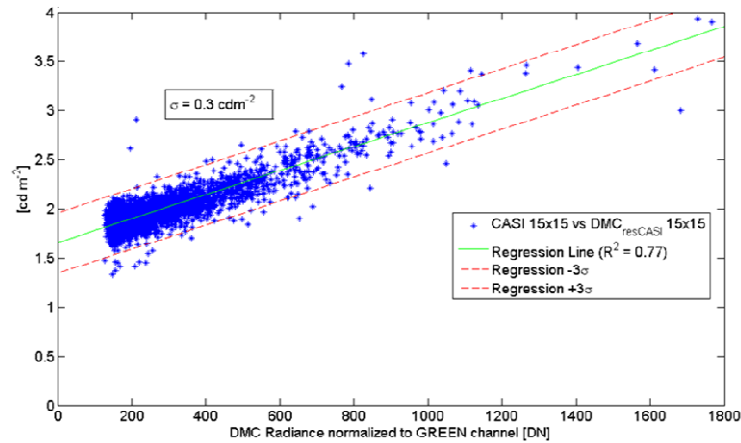

Figure 10 DMC green and blue optimum combination vs degraded CASI-550 luminous flux information.

The low values of DN in panchromatic images may cause the almost permanent failure of virtual image generation process. In more than 90% of acquisitions, manufacturer's SW failed to generate the virtual image, leading to completely dark images. In order to overcome this issue, the geometric parameters of the virtual plane projection had to be extracted from the header of the few images that had been processed correctly by the standard processing chain. Afterwards, a handmade code carrying out the compensation for the camera geometric distortions and the virtual plane projection was implemented. The basic idea is sketched in Figure 8. Another consequence of pixels' low intensity was the appearance of band-dependent noise patterns related to the CCD read-out process and residual vignetting affecting both multispectral and panchromatic images. Accordingly, band-tailored spectral filtering procedures were implemented to eliminate these undesired effects. An example is given in Figure 9.

6. DMC-BASED LUMINANCE MAP

After corregistering multispectral and panchromatic bands, the values of exposure time and aperture corresponding to each DMC acquisition were used to carry out the radiometric calibration. Then, the DMC filter functions provided by the manufacturer were employed to estimate the atmospheric attenuation using ModTran5.0 (see Section 3). The direct comparison between DMC and CASI-550 information revealed the presence of non-negligible radiance difference. As a matter of fact, DMC is not foreseen as a remote sensing device and radiometric calibration procedure is more intended for a relative more than an absolute field-of-view equalization.

In the light of this result, a different strategy to achieve an absolute calibration of DMC multispectral and panchromatic information was pursued. First, the two collections were mosaicked separately. The main constraint of the mosaicking procedure was the minimization of the zenith observation angle. Then, multispectral radiance and CASI-based luminance

mosaics were compared. To reduce discrepancies due to possible different observation geometry, the two mosaics were upscaled to 45x45m^2 spatial resolution. All those pixels of the degraded CASI-based mosaic showing values higher then 5 cdm^{-2} were used to estimate the coefficients of linear combinations of DMC multispectral bands providing the best fit to the scattering-affected luminance map F_0 in the least square sense. In order to reduce the memory burden, radiances were normalized to the green band gain and casted from float to integer. The best result was obtained combining the information contained in the blue (B) and the green (G) bands. In Figure 10, it is shown the distribution of the DMC radiance combination upscaled at CASI spatial resolution (3m) versus the corresponding values of F_0 (scattering affected luminous flux). Note that a minim threshold of 150 DN was fixed to avoid flux dispersion for values close to 1.5cdm^{-2}. It is important to stress that F_0 and not F was used in order to achieve a more precise estimation of the two last terms in (4), whose sum was directly given by the regression line offset in Figure 10. The value of this offset was 1.6cdm^{-2}. Taking into account the 3σ uncertainties, the final offset removed to calculate F was 1.3cdm^{-2}.

The luminous flux at DMC multispectral spatial resolution was finally obtained as

$$F_{DMC-MS} = m_{MS}\left(DN_G + \frac{c_B}{c_G} DN_B \right) \tag{5}$$

where m_{MS} is the linear regression slope, C_B and C_G are the radiometric calibration coefficient of the bands blue and green calculated using the capture integration time and the aperture parameters.

The last step of the analysis dealt with the possibility to retrieve a luminance map at the panchromatic spatial resolution. In the beginning, classical pansharpening techniques were taken into consideration and applied to the DMC radiances, but all of them generated undesired geometrical artifacts which compromised the radiometric quality of the final result. Therefore, a strategy similar to the one used for the multispectral information was investigated. First, the panchromatic image was upscaled to the multispectral image resolution. Then, the linear combination of panchromatic (P), blue (B) and green (G) radiances which best fitted the F_{DMC-MS} map was looked for. Despite all the combinations (P+G, P+B+P+G+B) provided good agreements in terms of R^2, the one using P and G was found to minimized the geometrical artifacts too. Following the same rationale already described in (5), the luminance at the panchromatic spatial resolution was obtained as

$$F_{DMC-PAN} = m_{PAN}\left(DN_G^{UP} + \frac{c_P}{c_G} DN_P \right) \tag{6}$$

where m_{PAN} is the linear regression slope of PG-F_{DMC-MS} linear regression, C_P is the radiometric calibration coefficient of the panchromatic image, and DN_G^{UP} is green multispectral image downscaled to the panchromatic spatial resolution.

The three images shown Figure 11 provide a visual comparison of the luminance information retrieved at the three different spatial resolutions: 3m for CASI550, and 1m and 25cm for DMC multispectral and panchromatic information, respectively. The area selected for the analysis is a roundabout located on the outskirts north of Sant Cugat del Vallès. First of all, it must be stressed the noteworthy improvement in the quality of the images in terms of spatial resolution. The slight geometrical discrepancies between CASI and DMC are due to two main reasons: the different way the pushbroom and frame sensors observed the same pixels on the ground, and the coarser resolution of the hyperspectral sensor, which is expected to introduce some regular shape distortions. Yet, the details contained in the multispectral-based map, and much more in the panchromatic map, become extremely useful in order to activate any artificial illumination optimization strategy. The blurred description provided by CASI at 3m sharpens in the multispectral map, where single street lamps are detectable. The panchromatic map allows one to give a step further. In fact, it becomes feasible to move from the detection of the brightest return of the surface closest to point light source to the characterization of a wider crown around this bright spot, where the illumination decreases proportionally to the distance from the source. This is basically due to the higher dynamic range provided by the photogrammetric bands with respect to the hyperspectral sensors. Obviously, the reason lies in the much broader filters used by DMC with respect to CASI550, which let more photons illuminate the CCD and hence provide higher DNs values.

Concerning the luminance absolute estimation, the radiometric information was preserved in the DMC map generation process. This can be observed in Figure 11, but becomes clearer in the collection of images reported in Figure 12. In order to improve the discrimination of flux intensities, a classification based on F segmentation from 0.35 to 10cdm^{-2} was employed. Details about each class are available in the caption of Figure 12. Through the use of the new color palette, it is easy to verify that the information retrieved using the CASI for luminance values higher than 1.5cdm^{-2} has been preserved.
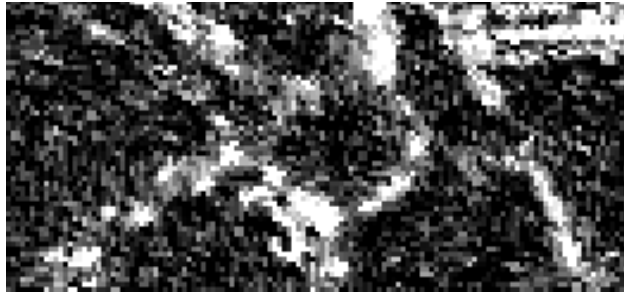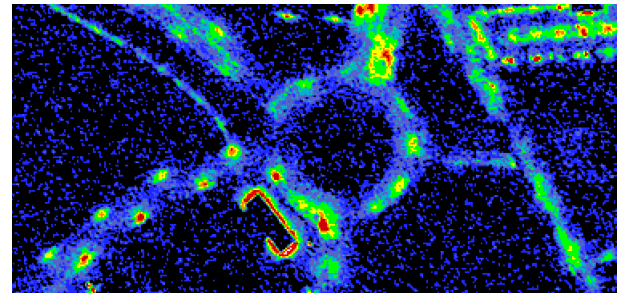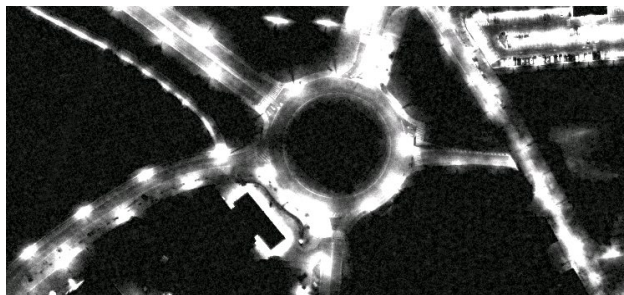
F CASI-550
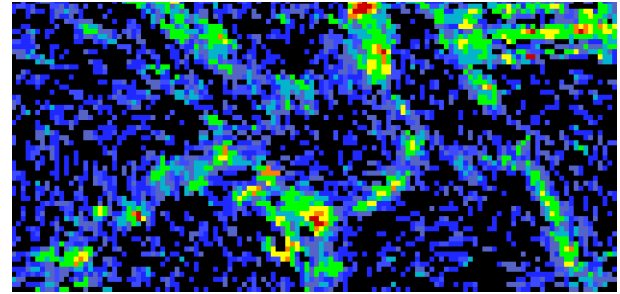
F CASI-550 Classification
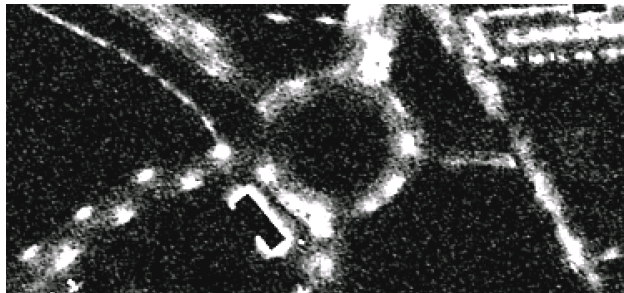
F DMC-MS

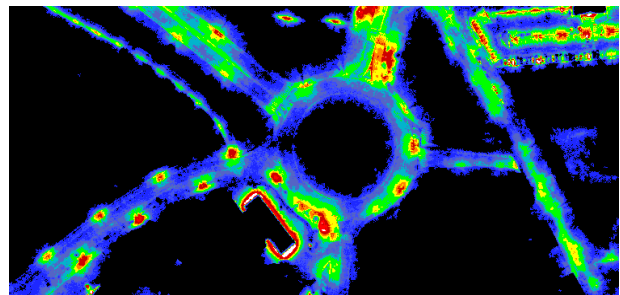F DMC-MS Classification

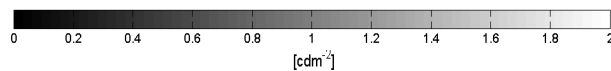
F DMC-PAN

F DMC-PAN Classification

Figure 11 CASI, DMC-MS and DMC-PAN Retrieved Luminous Flux F.

Figure 12 Classified CASI, DMC-MS and DMC-PAN Retrieved Luminous Flux F.

Moreover, the lower noise floor of DMC bands has enhanced the dynamic range of the retrieved luminance down to 0.65 cdm^{-2} and 0.35 cdm^{-2} using multispectral and panchromatic data, respectively.

In the CASI-based estimation of F described in Section 4, it was not possible to separated the scattering contribution K^{*} and noise contribution K_n, which summed up over non-illuminated areas. By the two-sensor fusion procedure, it can be stated that the atmosphere scattering contribution K_n, which is independent of the sensor, is lower than $0.35 cdm^{-2}$. The offset shown in Figure 10 is mainly due to the integration of the noise affecting each spectral band that sum incoherently during the photopic function synthesis, and must be properly compensated for to avoid overestimation of F. Conversely, the DMC data, after being calibrated using hyperspectral information, provide the opportunity to discriminate luminous flux

intensities down to those values that are often specified in legal regulations and should be monitored for efficient energy management policies.

7. METHODOLOGY PRELIMINARY ASSESSMENT

A rigorous assessment of the methodology put forward in this paper should be performed by comparing in-situ measurements acquired with a luminance meter simultaneously to the airborne acquisition process, and possibly with analogous observation parameters. Unfortunately, it was not possible to hold such a campaign in the period data had to be acquired. Yet, a preliminary estimation of the precision of the retrieved luminous flux was carried using non-simultaneous in-situ information. The measurements were acquired about 7 months earlier, on 9/7/2013 using a handheld CX-2A image luminance meter [18] by the CITELUM Iberica S.A, at the request of the municipality of Sant Cugat del Vallès. CITELUM has been the private company in charge of Sant Cugat del Vallès light street maintenance during the last years. Data were taken from a 10 meter aerial work platform with almost nadiral pointing angle, as shown in Figure 13. Four zones were measured using CX-2A, with two different points selected within each zone, corresponding to different types of asphalts (see Figure 14). A R8 GPS receiver with differential correction was used to determine with a few centimeter precision the XY position of a luminous reference point within the area imaged by the luminance meter. Once the pointing geometry was fixed, the reference was removed before taking the luminance measurement.

Despite the large time-gap between the two acquisition dates, it was meaningful to perform the comparison taking into account that the light sources are artificial. From the theoretical point of view, illumination conditions were expected to be stable if any bulb degradation or substitution is excluded, and no change in the surface reflectivity properties occurred. Unfortunately, CITELUM was not able to indicate the areas with in-situ information where these two main hypotheses were fulfilled.

Figure 13 Aerial work platform used for CX-2A acquisitions with.

Figure 14 Asphalt zones selected for the CX-2A acquisitions.

In order to compare the airborne and terrestrial measurement, an averaging square window whose size varied from 1 to 5 pixels was centered at the GPS coordinates, and the information luminance retrieved at the different spatial resolution was averaged.

The results are shown in Figure 15. It can be observed that the assumption that artificial illumination could be considered stationary over the 7 month time window is generally unfulfilled. The differences that are observable for zones 1A, 1B and 3A clearly indicate that either the light sources or the surface reflectivity properties must have changed significantly between the two acquisitions. On the contrary, the lower errors found for the rest of zones 2A nd 4B seem to indicate that slight changes took place between July 2013 and February 2014.
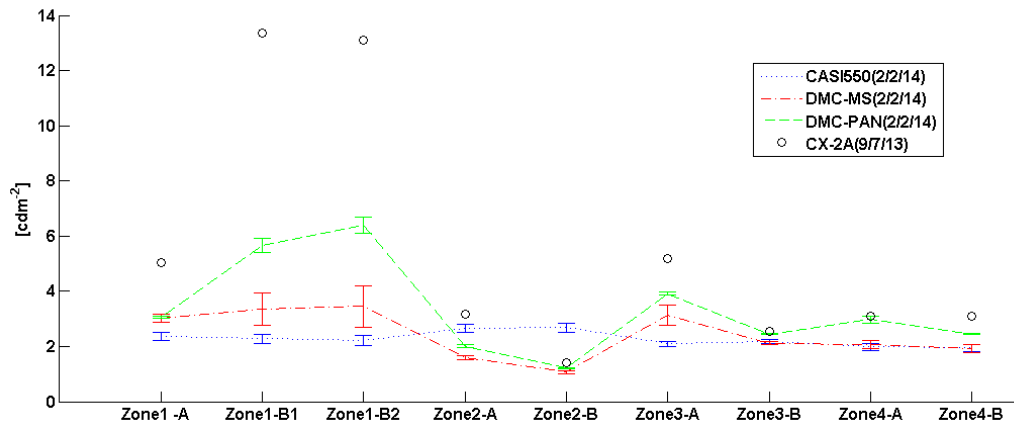
Figure 15 Luminance parameter retrieved via CASI and DMC (multispectral and panchromatic) images versus non-simultaneous (7 month time-span) in-situ measurements.

Equally, the differences may be ascribed in some measure to airborne estimation errors but even to ground-truth uncertainty. According to CX-2A specification, luminance meter accuracy is about 5% errors. At the same time, observation geometry and spatial resolution differences are expected to play a key role in luminance retrieval, as it is shown by the simultaneous CASI and DMC data.

Indeed, the lowest differences between in-situ measurements and luminance map are observed for the panchromatic case, for which the observation geometry in terms of pointing angle and spatial resolution is most resembling. The estimation of luminance for zones 2B, 3B and 4A provided by the DMC-PAN map matches the in-situ measurements with an error lower than $0.2 cdm^{-2}$.

Concluding, despite all the aforementioned drawbacks and limitations, this preliminary validation demonstrates the effectiveness of the methodology here proposed, and encourages holding a new campaign with in-situ measurements (and possibly a radiosounding) simultaneous to the airborne acquisition process to carry out a rigorous assessment of the whole procedure. Finally, these results are also important because demonstrate that, if radiometrically cross-calibrated using simultaneous hyperspectral information, the photogrammetric camera DMC may be operated as a remote sensing device for physical parameter quantitative estimation.

8. CONCLUSIONS

In this paper, the methodology developed at the Institut Cartogràfic i Geològic de Catalunya (ICGC) to quantify upwelling light flux using hyperspectral airborne data has been proposed. Nocturnal hyperspectral data acquired over the municipality of Sant Cugat del Vallès (Spain) have been processed to generate the luminance map of the flown area. In order to overcome CASI spatial resolution and radiometric sensitivity limitations, DMC data acquired simultaneously to the hyperspectral information have been used in a multi-sensor approach. As a result, high-resolution (HR) luminance maps with enhanced sensitivity were retrieved. The study has demonstrated the feasibility to use photogrammetric sensors for remote sensing applications whenever the radiometry of these imaging devices can be trusted. To this end, the cross-calibration procedure based on simultaneous hyperspectral acquisitions proposed in this paper represents a feasible as well as operative solution. A preliminary assessment with non-simultaneous (7 month time span) in-situ measurements has been carried out to provide a first demonstration of the effectiveness of the proposed methodology. In the next future, simultaneous airborne and in-situ measurements, and possiblly a radiosounding, will be carried out in collaboration with the municipal administration of Sant Cugat for a more rigorous assessment. Being aware of the key importance of geometrical parameters, in-situ data will be acquired again from an aerial work platform to reproduce airborne observation conditions.

9. ACKNOWLEDGMENT

REFERENCES

[1] CIE, "CIE Commission Internationale de l'Eclairage Proceedings", Cambridge University Press, (1931).

[2] CIE, "CIE data of 1931 and 1978" < http://www.cvrl.org/>.

[3] Aubé, M., Franchomme-Fossé, L., Robert.Staehler, P., Houle, V., "Light Pollution Modelling and Detection in a Heterogeneous Environment," Proceedings of SPIE 5890. Atmospheric and Environmental Remote Sensing Data Processing and Utilization, (2005).

[4] Tardà A., Palà V., Arbiol, R, Pérez F., Viñas O., Pipia L., et al., "Detección de la iluminación exterior urbana nocturna con el sensor aerotransportado CASI-550," Internation Geomatic Week, Barcelona, Spain, (2011).

[5] Elvidge, C.D., Keith, D.M., Tuttle, B.T., Baugh, K.E., "Spectral Identification of Lighting Type and Character," Sensors 10,3961-3988, (2010).

[6] Barducci, A., Benvenuti, M., Bonora, L., Castagnoli, F., Guzzi, D., Marcoionni P., Pippi, I., "Hyperspectral remote sensing for light pollution monitoring," Annals of Geophysics vol. 49(1), 305-310, (2006).

[7] Elvidge C.D, Baugh K.E., Kihn E.A, Kroel H.W., and Davis E.R., "Mapping City Lights With Nighttine Data from the DMSP Operational Linescan System," Photogrammetric Engineering and Remote Sensing, Vol 63, Issue 6, pp 727-734 (1997).

[8] Small, C., Pozzi, F., Elvidge, C.D., "Spatial analysis of global urban extent from DMSP-OLS night lights," Remote Sensing of Environment 96, 277-291, (2005).

[9] Miller S.D., Straka, W., Mills S.P., Elvidge C.D. at al., "Illuminating the Capabilities of the Suomi National Polar-Orbiting Partnership (NPP) Visible Infrared Imaging Radiometer Suite (VIIRS) Day/Night Band," Remote Sensing, Vol. 5, pp 6717-6766 (2013).

[10] Levin N., Johansen K., Hacker J.M., Phinn S., "A new source for high spatial resolution night time images- The EROS-B commercial satellite," Remote Sensing of Environment, 140 (2014).

[11] ITRES, "CASI550 Manufacturer data sheet", < http://www.itres.com/assets/pdf/CASI-550.pdf>.

[12] M. Aubé, "Light Pollution Modelling and Detection in a Heterogeneous Environment," Starlight, a Common Heritage, (2008).

[13] Berk, A.E., "MODTRAN 5: A Reformulated Atmospheric Band Model with Auxiliary Species and practical Multiple Scattering options", Proceedings of the SPIE 5806, 662-667,(2005).

[14] Barsi, J.B., "An Atmospheric Correction Parameter Calculator for a Single Thermal Band Earth-Sensing Instrument," IGARSS03 Toulouse, France (2003).

[15] Catalonian Automatic Weather Station Network (XEMA): http://www.meteo.cat/xema/.

[16] National Physical Laboratory: http://www.npl.co.uk/.

[17] Dörstel, C., "DMC- Practical Experiences and Photogrammetric System Performance," Proceedings of the 49th PhoWo, 59-65, (2003).

[18] CX-2 Imageing Luminance meter: http://www.everfine.net/productinfo.php?pid=14&clid=9